

# Ultraviolet Signatures of Jet–Ejecta Interaction in Early Kilonovae: Prediction from Realistic Atomic Opacities

SMARANIKA BANERJEE ,<sup>1</sup> HAMID HAMIDANI ,<sup>2</sup> KYOHEI KAWAGUCHI ,<sup>3</sup> AND MASAOMI TANAKA ,<sup>2,4</sup>

<sup>1</sup>*Institut für Kernphysik, Technische Universität Darmstadt, Schlossgartenstr. 2, 64289 Darmstadt, Germany*

<sup>2</sup>*Astronomical Institute, Tohoku University, Aoba, Sendai 980-8578, Japan*

<sup>3</sup>*Max Planck Institute for Gravitational Physics (Albert Einstein Institute), Am Mühlenberg 1, Potsdam-Golm, 14476, Germany; Center of Gravitational Physics and Quantum Information, Yukawa Institute for Theoretical Physics, Kyoto University, Kyoto, 606-8502, Japan*

<sup>4</sup>*Division for the Establishment of Frontier Sciences, Organization for Advanced Studies, Tohoku University, Sendai 980-8577, Japan*

(Received; Revised; Accepted January 29, 2026)

## ABSTRACT

We investigate the signature of the jet–ejecta interaction in early kilonova ( $t \leq 1$  day) using detailed atomic opacities developed in Banerjee et al. (2020, 2024), appropriate for early times ( $t \sim 1$  hour after the merger). We explore jets with different powers and opening angles. We find that the presence of the jet shifts the spectral peak to longer wavelengths, with the strongest effect near the polar viewing angle. This occurs because the jet creates a thin, low-density outer layer ahead of the bulk ejecta. The opacity of this layer can be as high as  $\kappa \sim 200 \text{ cm}^2 \text{ g}^{-1}$ , causing photons to escape from cooler, faster-moving outer layer rather than from the hot inner ejecta. The bolometric light curves likewise exhibit a clear imprint of the jet–ejecta interaction, showing suppressed early-time luminosity near polar viewing angles compared to the equatorial one, as the photosphere resides in this thin layer where radioactive heating is lower than in the bulk ejecta. These signatures are also evident in multi-color light curves, particularly in the ultraviolet and  $u$ -bands. For example, in the *Swift* UVW2 band at  $t \simeq 0.15$  days for a source at 100 Mpc, the ultraviolet luminosities can reach  $\sim 19.5$  mag if no jet is present, while the presence of the jet can make it fainter by  $\sim 2.5$  mag. The strongest observational signature occurs in the *UVEX* NUV, *Swift* UVW2, and UVM2 bands, which remains detectable out to viewing angles of  $\sim 60^\circ$  for  $t \lesssim 1$  days. Rapid follow-up with future ultraviolet facilities, such as *ULTRASAT* and *UVEX*, will provide powerful probes of jet–ejecta interaction through early-time kilonova observations.

*Keywords:* Neutron star, opacity, atomic calculation, kilonova

## 1. INTRODUCTION

On August 17, 2017, the first binary neutron star merger was detected via the multimessenger signal, simultaneously in gravitational waves (GW170817, Abbott et al. 2017) and electromagnetic counterparts across the spectrum. The electromagnetic signal includes the short ( $T_{90} \leq 2$  s) gamma-ray burst (GRB170817A, e.g., Connaughton et al. 2017; Savchenko et al. 2017; Tanvir et al. 2017) and the kilonova, the transient powered by the freshly synthesized heavy elements (e.g., Li & Paczyński 1998; Metzger et al. 2010), AT2017gfo (e.g., Coulter et al. 2017; Yang et al.

2017; Valenti et al. 2017; Cowperthwaite et al. 2017; Smartt et al. 2017; Drout et al. 2017; Utsumi et al. 2017).

This observation has marked the watershed moment in many aspects; for example, the detection of the kilonova confirms that these are one of the sites of heavy elements synthesis, proving theoretical predictions (e.g., Lattimer & Schramm 1974; Eichler et al. 1989; Freiburghaus et al. 1999; Korobkin et al. 2012; Wanajo et al. 2014). Moreover, the discovery also validates the long-standing hypothesis regarding these mergers to be connected with short GRBs (e.g., Eichler et al. 1989; Paczynski 1991). In the following years, additional kilonova candidates have been reported in association with both short and long-duration ( $T_{90} > 2$  s) GRBs, including GRB 211211A (e.g., Rastinejad et al. 2022) and GRB 230307A (e.g., Levan et al. 2024). These

**Table 1.** Summary of the jet-interacted ejecta models adopted from Hamidani & Ioka (2023a,b). In all cases, the jet is assumed to remain active for 2 s. The bulk ejecta into which the jet is launched follows a power-law density profile with index  $-2$ . The table lists, from left to right: the model names (defined by the jet power and opening angle); the isotropic-equivalent luminosity of the jet engine,  $L_{\text{iso}} = \frac{2L_j}{1 - \cos \theta_j} \simeq 4L_j/\theta_j^2$ , where  $L_j$  is the true (one-sided) jet power; the initial jet opening angle  $\theta_j$ ; the outcome of whether the jet hydrodynamically breaks out of the ejecta; and the mass of the thin outer layer, defined as the ejecta/cocoon mass with velocities larger than the edge of the bulk ejecta.

Model name	$L_{\text{iso}}$ [erg s $^{-1}$ ]	$\theta_j$ [°]	Jet successfully broke out?	$M(> v_{\text{ej,max}})$ [ $M_{\odot}$ ]
PL	—	—	—	—
HE-NJ	$5 \times 10^{50}$	6.8	Yes	$2.1 \times 10^{-5}$
LE-NJ	$1 \times 10^{50}$	6.8	Yes	$2.0 \times 10^{-5}$
HE-WJ	$5 \times 10^{50}$	18.0	Yes	$1.1 \times 10^{-4}$
LE-WJ	$1 \times 10^{50}$	18.0	No	$5.9 \times 10^{-5}$

events further support the picture in which relativistic jets are launched following compact object mergers.

Although the association between compact object mergers and relativistic jet launching is now well established, the precise timing of jet formation remains uncertain. For instance, jet launching may be delayed if the magnetic field around the central compact object requires time to amplify to the strength necessary to drive a relativistic outflow (e.g., Lazzati 2020). In such scenarios, the jet propagates through merger ejecta that have already been launched and have started expanding. As the jet drills through the dynamical ejecta, it reshapes the density and angular structure of the outflow (e.g., Duffell et al. 2018; Hamidani et al. 2020; Nativi et al. 2021; Hamidani & Ioka 2023a,b).

Previous studies have shown that these jet-induced modifications to the ejecta can leave observable imprints on kilonova emission (Klion et al. 2021; Nativi et al. 2021; Shrestha et al. 2023). However, these studies are limited by their use of approximate treatments of the microphysics. During the photospheric phase, the emergent light curves and spectra are primarily governed by the wavelength- and time-dependent opacity of the ejecta, which is determined by the atomic properties of the freshly synthesized  $r$ -process elements (e.g., Metzger et al. 2010; Kasen et al. 2013; Tanaka & Hotokezaka 2013). Consequently, reliable predictions of kilonova emission demand accurate atomic opacities that consistently capture the evolving thermodynamic and ionization conditions of the expanding ejecta.

At early times, the ejecta are dense and have high temperature. For a GW170817-like kilonova, temperatures can reach  $T \sim 10^5$  K at  $t \sim 1$  hour after merger (Banerjee et al. 2020, 2022), leading to highly ionized material, with charge states reaching up to XI (Banerjee et al. 2020). Modeling the early-time emission, therefore, requires time- and wavelength-dependent opacities for highly ionized heavy elements. However, previous studies of jet-ejecta interaction effects on kilonova light

curves have relied on simplified opacity treatments. For example, Klion et al. (2021) employed a gray-opacity approximation, while Nativi et al. (2021) adopted analytic prescriptions based on low-ionization (I-IV) opacities of a limited set of  $r$ -process elements (Tanaka et al. 2018). More recently, Shrestha et al. (2023) used detailed opacities for elements from Ca - Ra ( $Z = 20 - 88$ , Tanaka et al. 2020), but restricted to ionization states up to IV. As demonstrated by Banerjee et al. (2020, 2022, 2024), such treatments are insufficient for the earliest epochs ( $t \lesssim 1$  day), when higher ionization stages dominate the opacity.

In this paper, we present kilonova light curves from jet-interacted ejecta in binary neutron star mergers, employing the atomic opacities of Banerjee et al. (2020, 2024) that are appropriate for the early phase ( $t \leq 1$  day). For the jet-interacted ejecta models, we adopt the calculations from Hamidani & Ioka (2023a,b). The structure of the paper is as follows: in Section 2, we describe the ejecta structure after modification by the jet; in Section 3, we provide details of the radiative-transfer simulations; in Section 4, we present the results; in Section 5, we discuss the detectability of kilonova light curves relative to the afterglow and compare our findings with previous works; and finally in Section 6, we summarize our conclusions. All magnitudes in this paper are given in the AB system.

## 2. EJECTA STRUCTURE

To model the kilonova emission from jet-modified ejecta in neutron star mergers, we use the two-dimensional hydrodynamical simulations that follow the propagation of relativistic jets through merger ejecta (Hamidani & Ioka 2023a,b). These simulations provide a physically motivated description of the jet-ejecta interaction and allow us to reconstruct the resulting outflow geometry and composition. The initial conditions, post-processing procedures, and the ejecta structures adopted for our radiative-transfer calculations are de-

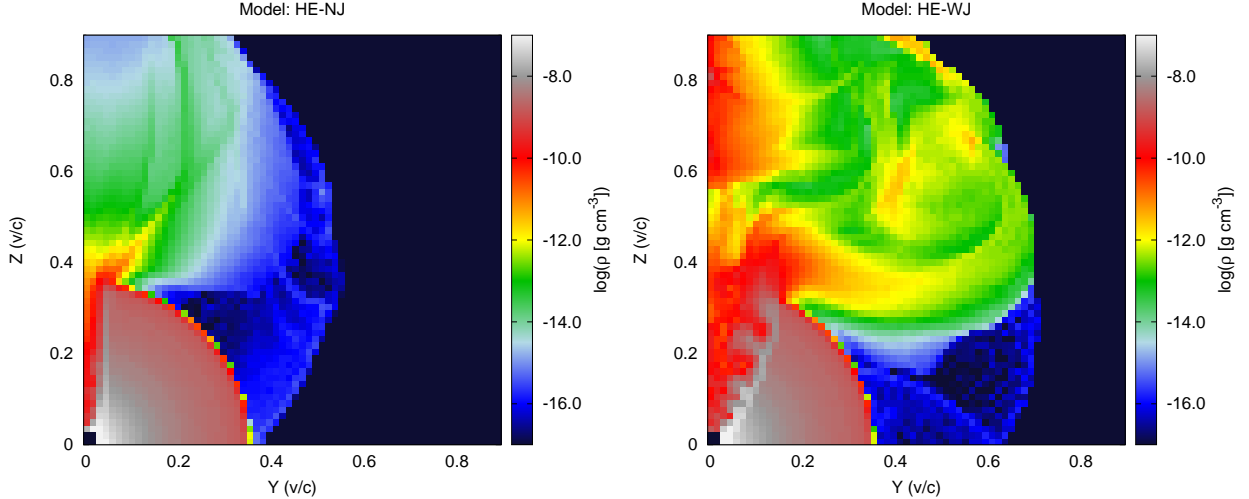


**Figure 1.** Two-dimensional ejecta structures for different models at  $t = 0.03$  days, which is the starting point of our radiative-transfer simulations. The hydrodynamic simulation results are post-processed by mapping them onto an axisymmetric velocity grid with the resolution adopted for the radiative-transfer calculations. Moreover, we exclude all material with  $v > 0.9c$ . **Left:** ejecta after interaction with the narrow jet (NJ); **Right:** ejecta after interaction with the wide jet (WJ). Only the high-luminosity jet models (HE) are shown here. The jet–ejecta interaction produces a thin layer at the leading edge of the ejecta, particularly along the polar direction, while the equatorial regions, being far from the jet core, remain largely unaffected. The black central region denotes material with  $v < 0.025c$ . This component is omitted from our simulations, as its low mass and extreme optical depth make its contribution to the early-time light curves negligible.

scribed in the following subsections. A more detailed account of the computational methods underlying these simulations can be found in Hamidani & Ioka (2023a) and Hamidani & Ioka (2023b).

### 2.1. Jet initial conditions

In hydrodynamical simulations, the jet is assumed to be launched as a consequence of accretion onto the newly formed central compact object. The exact jet launch time depends on the formation timescale, nature, and properties of the remnant, all of which remain uncertain (e.g., Kiuchi et al. 2019, 2023). For simplicity, we adopt a fiducial launch time of  $\simeq 0.16$  s after the merger, consistent with the setup in Hamidani & Ioka (2023a,b). This choice is also compatible with observational constraints from GRB170817A, which require  $t_{\text{launch}} \leq 1.3$  s once the jet breakout time is taken into account (Hamidani et al. 2020). We further assume that the central engine remains active for  $\sim 2$  s, consistent with both the typical duration of short GRBs (e.g., Kouveliotou et al. 1993) and the observed duration of GRB170817A (e.g., Goldstein et al. 2017).

We investigate a set of jet models by varying both jet power and opening angle. The jet initial opening angle is considered to be  $\theta_j = 6.8^\circ$  and  $\theta_j = 18^\circ$  (NJ and WJ models), motivated by the range of opening angles typically inferred for GRBs (e.g., Fong et al. 2015; Rouco Escorial et al. 2023). Similarly, the isotropic-equivalent luminosity of the jet is assumed to be  $L_{\text{iso}} =$

$10^{50}$  and  $5 \times 10^{50}$  erg s $^{-1}$  (LE and HE models), consistent with the characteristic energy range observed in GRBs (Fong et al. 2015). A summary of the adopted models is provided in Table 1.

### 2.2. Initial ejecta structure

After its launch, the jet propagates through the merger ejecta, modifying its structure along the way. This interaction is most pronounced in the polar regions, where the ejecta is strongly affected. For the jet-launch timescale adopted in this work, i.e.,  $t_{\text{jet}} = 0.16$  s after the merger, these regions are assumed to be dominated by post-merger ejecta (e.g., Fujibayashi et al. 2018, 2020c). Motivated by this picture, we model the ejecta as a steady wind-driven outflow from the accretion disk, resulting in a power-law density profile,

$$\rho(r) = \rho_0 \left( \frac{r}{r_0} \right)^{-2}, \quad (1)$$

where  $r_0 \sim 1.2 \times 10^8$  cm is the inner boundary of the hydrodynamical simulations. The density at this boundary is given by

$$\rho_0 = \frac{M_{\text{ej}}}{4\pi r_0^2 (r_{\text{max}} - r_0)}.$$

Here  $r_{\text{max}} = v_{\text{max}} t_0$  and  $t_0 \simeq 0.16$  s. The ejecta velocity range is taken to be  $v_{\text{ej}} = 0.025c$  to  $0.35c$ . The upper limit is motivated by root mean squared velocities from previous simulations (e.g., Hotokezaka et al. 2013).

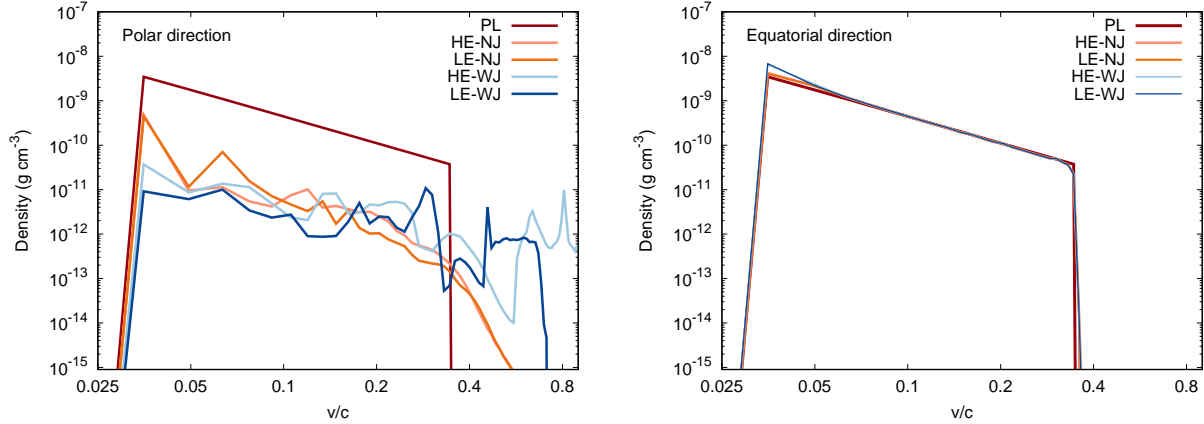


**Figure 2.** One-dimensional ejecta structures for all models shown in Table 1 at  $t = 0.03$  days, marking the starting point of our radiative-transfer simulations, shown along the polar ( $\theta_v = 0 - 14^\circ$ , left) and equatorial ( $\theta_v = 88 - 90^\circ$ , right) directions. Different colors indicate different models, including the PL model without jet interaction. Both the narrow- and wide-jet cases (NJ and WJ) exhibit significant modifications to the density structure relative to the PL model, most prominently along the polar direction. In both cases, a thin layer develops at the leading edge of the polar ejecta, while the equatorial ejecta remains largely unchanged. For the narrow-jet models (HE-NJ and LE-NJ), this layer follows a steeply declining power-law-like profile, whereas in the wide-jet models, the density distribution differs owing to the broader interaction induced by the larger opening angle.

We adopt the total ejecta mass to be  $M_{\text{ej}} = 0.01M_\odot$ . This lies on the lower end of typical disk wind ejecta mass. However, the mass adopted here is good enough to represent the earlier jet-propagated ejecta environment, when the majority of the emission appears from the outermost layer. Hence, we consider such ejecta structure, since the early-time ( $t \leq 1$  day) kilonova is the major focus of this work.

### 2.3. Post-processing the ejecta

In the hydrodynamic simulations adopted from Hamidani & Ioka (2023a,b), the evolution of the jet and ejecta is followed up to  $t - t_0 \sim 10$  s after the merger, as the hydrodynamic calculations are computationally expensive. Within this time span, the ejecta have not yet reached homologous expansion, in which the velocity field satisfies  $v = r/t$ . Since homologous expansion is a key assumption in our radiative-transfer calculations, we therefore post-process the ejecta to extrapolate its structure to later times, when the homologous phase is established.

For the post-processing of the ejecta, we start from the final snapshot of the hydrodynamic simulations ( $t - t_0 \sim 10$  s). From this snapshot, we extract the fluid properties in each grid cell, including the rest-mass density, velocity, and specific enthalpy ( $h$ ). We then extrapolate these quantities to later times, assuming that sufficiently after jet breakout the fluid elements evolve ballistically, without further interactions, and undergo only adiabatic expansion. In this regime, the velocity of each fluid element asymptotically approaches terminal velocity,  $v_\infty \simeq c\sqrt{1 - \Gamma_\infty^{-2}}$ , where the terminal Lorentz factor

is given by  $\Gamma_\infty \simeq h\Gamma$ , following Bernoulli's law. We evolve the system to  $t \sim 10^3$  s after the merger, by which time the ejecta have reached homologous expansion. Finally, the post-processed ejecta are mapped from the high-resolution hydrodynamical grid ( $512 \times 9200$ ) onto the radiative-transfer grid ( $64 \times 64$ ) to obtain the ejecta structure used in our simulations.

### 2.4. Final ejecta structure

Figure 1 shows the two-dimensional density structure of the ejecta at  $t = 0.03$  days, the starting point of our radiative-transfer simulations. The left and right panels correspond to models in which the ejecta interact with a narrow and a wide jet (NJ and WJ), respectively. For simplicity, only the ejecta interacted with the high-luminosity jets ( $L_{\text{iso}} = 5 \times 10^{50}$  erg s $^{-1}$ ; HE models) are shown. We impose a maximum ejecta velocity limit of  $v_{\text{ej}} = 0.9c$ , which does not affect the radiative-transfer results since the mass beyond this limit is negligible ( $M_{v_{\text{ej}} > 0.9c} \lesssim 10^{-6}M_\odot$ ; Hamidani & Ioka 2023a,b).

In both narrow and wide jet cases (HE-NJ, HE-WJ), the jet-ejecta interaction significantly alters the structure, producing a thin layer ahead of the bulk ejecta, most prominently along the polar direction. By contrast, modifications in the equatorial direction are minimal, consistent with its large angular separation from the jet core.

A high-density polar plug is visible in the density maps, most prominently in the wide-jet case at velocities  $v_{\text{ej}} > 0.6c$ . This feature arises from the 2D axisymmetric approximation in the hydrodynamic simulations and may affect the jet dynamics. Considering that this plug

consists of fast-moving outflow ( $v_{\text{ej}} > 0.6c$ ) confined to the vicinity of the jet axis ( $\lesssim 10^\circ$ ), its presence (i.e., high density) may influence the very early-time KN emission ( $\lesssim 0.1$  day or  $\lesssim 2$  hours) for observers with a line of sight aligned with the jet axis. However, its impact on the later epochs ( $t \gtrsim 0.1$  days) should be non-significant.

To compare the ejecta structure across models, we show the one-dimensional ejecta profiles for all models, including the power-law (PL) model without jet interaction (Table 1), at  $t = 0.03$  days in Figure 2. The figure displays the density distributions along both the polar (left) and equatorial (right) directions.

The jet-interacted ejecta models exhibit significantly modified density profiles, especially along the polar direction. At velocities below the fiducial maximum of the wind ejecta ( $v_{\text{ej}} < 0.35c$ ), the densities are reduced, with the displaced inner material redistributing into a thin outer layer up to a higher velocity, with the exact value depending on the model. In the narrow-jet cases (NJ), the density of this layer declines steeply with velocity, while in the wide-jet cases (WJ), the density structure becomes more complex owing to the interaction happening in the broader region of the ejecta. Along the equatorial direction, the density profiles remain largely unchanged, with only minor variations in the innermost regions across different models, and their peak values remain close to those of the PL model. Note that we see a sharp drop in the inner and outer boundary due to the initial density chosen as the power-law structure (Equation 1).

### 3. RADIATIVE TRANSFER SIMULATIONS

Using the density structures described in Section 2, we model the kilonova emission from  $t = 0.03$  days with a time- and wavelength-dependent Monte Carlo radiative-transfer code (Tanaka & Hotokezaka 2013; Tanaka et al. 2018; Kawaguchi et al. 2018, 2021). The code computes the light curves and spectra, given the density distribution, elemental abundances, and radioactive heating rate.

#### 3.1. Abundances

In a neutron star merger, masses are ejected in several different channels (Shibata & Hotokezaka 2019), producing multiple ejecta components, each of which has a different electron fraction ( $Y_e$ ), i.e., the electron to baryon ratio in the ejecta. For example, tidal dynamical ejecta, which is the mass ejected within the dynamical timescale due to the tidal disruption, has relatively lower electron fraction  $Y_e < 0.25$ , whereas the polar dynamical ejecta, which is the ejecta emitted towards the polar direction due to the shock between the interface of

the neutron stars have relatively higher electron fraction  $Y_e > 0.25$  (e.g., Bauswein et al. 2013; Just et al. 2015; Sekiguchi et al. 2015; Just et al. 2022). In addition, mass outflows from the accretion disk formed around the central remnant, which are ejected more isotropically, exhibit a broad range of electron fractions,  $Y_e$  (e.g., Fernández & Metzger 2013; Metzger & Fernández 2014; Miller et al. 2019; Fernandez & Metzger 2014; Perego et al. 2014; Lippuner et al. 2017; Fujibayashi et al. 2018, 2020a,c,b).

In this work, we consider mainly the disk wind part of the ejecta, through which the jet moves after getting launched at  $t - t_0 = 0.16$  s (see Section 2). We adopt the electron fraction to be  $Y_e = 0.30 - 0.40$ , consistent with the possible  $Y_e$  range in the disk wind ejecta. We take elemental abundances and heating rates from the  $r$ -process nucleosynthesis results of Wanajo et al. (2018). A flat mass distribution is assumed across the range of  $Y_e$  values. For the sake of simplicity, we assume the  $Y_e$  to be the same and the abundances are homogeneous throughout the ejecta.

#### 3.2. Heating

The ejecta from a compact-object merger can be heated through multiple channels, including (i) the radioactive decay of freshly synthesized  $r$ -process nuclei, (ii) shock or cocoon heating resulting from jet–ejecta interaction, and (iii) energy injection from sustained central-engine activity (see Metzger 2020). In this work, we neglect any long-term central-engine contribution and compare only the first two mechanisms as potential heating sources.

The thermal energy input from radioactive decay overwhelmingly exceeds that from cocoon-induced shock heating. This can be demonstrated with a simple order-of-magnitude estimate. The thermal energy deposited by the cocoon is given by  $\eta_{\text{coc}} E_{\text{coc,th}}$ , where  $E_{\text{coc,th}} \simeq 2L_j t_{\text{bo}}$ , with the jet breakout time  $t_{\text{bo}} \simeq 0.4$  s. We adopt a cocoon thermalization efficiency of  $\eta_{\text{coc}} \simeq 0.5$  by following Hamidani et al. (2020). For the wide-jet model (HE-WJ) with an opening angle of  $\theta_j = 18^\circ$ , and adopting a jet power  $L_j \simeq L_{\text{iso}} \theta_j^2 / 4 \simeq 1.2 \times 10^{49}$  erg s $^{-1}$ , we obtain a cocoon thermal energy of  $E_{\text{coc,th}} \sim 10^{44}$  erg at  $t \sim 1$  hour.

By contrast, the energy released through radioactive decay of freshly synthesized  $r$ -process nuclei is far larger. The specific heating rate approximately follows  $\dot{E} \propto t^{-1.3}$  erg s $^{-1}$  g $^{-1}$  (Metzger et al. 2010). For an ejecta mass of  $M_{\text{ej}} = 0.01 M_\odot$ , the total radioactive energy deposited within the first hour is  $E_{\text{rad}} \sim 10^{48}$  erg, assuming a thermalization efficiency of  $\eta \simeq 0.5$ . Thus, radioactive heating exceeds the cocoon contribution by

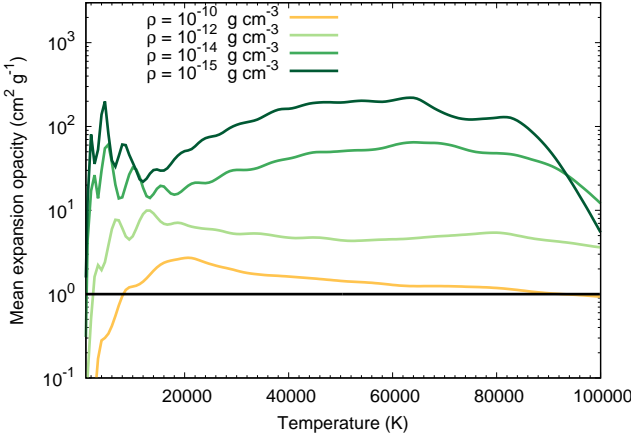


**Figure 3.** Opacity evolution with temperature for different densities at  $t = 0.1$  days taken from [Banerjee et al. \(2020, 2024\)](#). The black line shows the gray opacity adopted by most earlier works (e.g., [Klion et al. 2021](#)).

roughly three to four orders of magnitude, consistent with previous studies (e.g., [Klion et al. 2021](#)).

Given that radioactive heating dominates the energy budget, we neglect any contribution from jet-induced shock heating and include only radioactive heating. The thermalization efficiency of the decay products is computed using the analytic prescription of [Barnes et al. \(2016\)](#). We include the radioactive energy deposition prior to the initial epoch by accounting for its degradation due to adiabatic cooling.

### 3.3. Ejecta physical state

In the expanding ejecta of a neutron star merger, the physical conditions, such as density and temperature, and consequently the opacity, evolve with time. For instance, the density drops as  $\rho(r, t) \propto t^{-3}$  under homologous expansion. Correspondingly, the temperature and opacity evolve. The Monte Carlo radiative-transfer code used in this work accounts for these effects self-consistently. In the following, we briefly outline how the temperature and opacity are determined at each timestep of calculation, while further details can be found in [Tanaka & Hotokezaka \(2013\)](#); [Kawaguchi et al. \(2018, 2021\)](#).

The temperature is determined from the photon flux, under the assumption that the electron temperature is equal to the radiation temperature. The photon intensity is first calculated in individual cells after the photon transfer ([Lucy 2003](#); [Tanaka & Hotokezaka 2013](#)):

$$J_\nu = \frac{1}{4\pi\Delta t V} \sum_{d\nu} \epsilon ds, \quad (2)$$

where the summation is over the photon trajectory segment,  $ds$ , for the photons in the discretized cell of volume  $V$ , with the comoving energy  $\epsilon$ , over the timesteps  $\Delta t$ . This intensity is then integrated over frequency to calculate  $\langle J \rangle = \int J_\nu d\nu$ , which is related to the temperature as per Stefan-Boltzmann law,  $\langle J \rangle = \sigma T^4 / \pi$ . This treatment is adopted from [Kromer & Sim \(2009\)](#).

The density and temperature control the ionization state and atomic level populations of the ejecta, and therefore determine the opacity. The opacity influences the photon propagation in the ejecta, hence the light curves and spectra of the kilonova. Here, we mainly discuss the bound-bound opacity, which makes the dominant component in the neutron star merger ejecta in the early time. In the case of supernovae and neutron star mergers, where the matter is expanding with a high velocity and a high velocity gradient, we use the expansion opacity formalism ([Sobolev 1960](#); [Pinto & Eastman 2000](#)) as:

$$\kappa_{\text{exp}}(\lambda) = \frac{1}{\rho c t} \sum_l \frac{\lambda_l}{\Delta\lambda} (1 - e^{-\tau_l}), \quad (3)$$

where  $\lambda_l$  is the transition wavelength in the wavelength interval of  $\Delta\lambda$  and  $\tau_l$  is the Sobolev optical depth at the transition wavelength, calculated as

$$\tau_l = \frac{\pi e^2}{m_e c} n_l \lambda_l f_l t. \quad (4)$$

Here  $f_l$  is the strength of transition and  $n_l$  is the number density of the lower level of the transition, evaluated by the Boltzmann distribution:

$$n_l = \frac{g_l}{U(T)} \exp(-E_l/kT), \quad (5)$$

where  $g_l$  and  $E_l$  are the statistical weights and the excited energy of the lower level, respectively, and  $U(T)$  is the partition function of the ion.

We perform the radiative-transfer calculations under the assumption of local thermal equilibrium (LTE). Hence, we solve the Saha ionization equation to calculate the ionization fraction. Previous studies ([Kasen et al. 2013](#); [Banerjee et al. 2022](#)) have shown that this approximation is valid for the first few days after the merger. Since our focus is on very early times ( $t \leq 1$  day), this treatment is appropriate.

[Figure 3](#) shows the Planck mean expansion opacity as a function of temperature for several representative ejecta densities (see [Figure 2](#)) at  $t \sim 0.1$  days. The opacities are calculated for an electron fraction of  $Y_e = 0.30\text{--}0.40$ , i.e., the lanthanide-free elemental compositions ( $Z = 20 - 56$ ) over the wavelength range

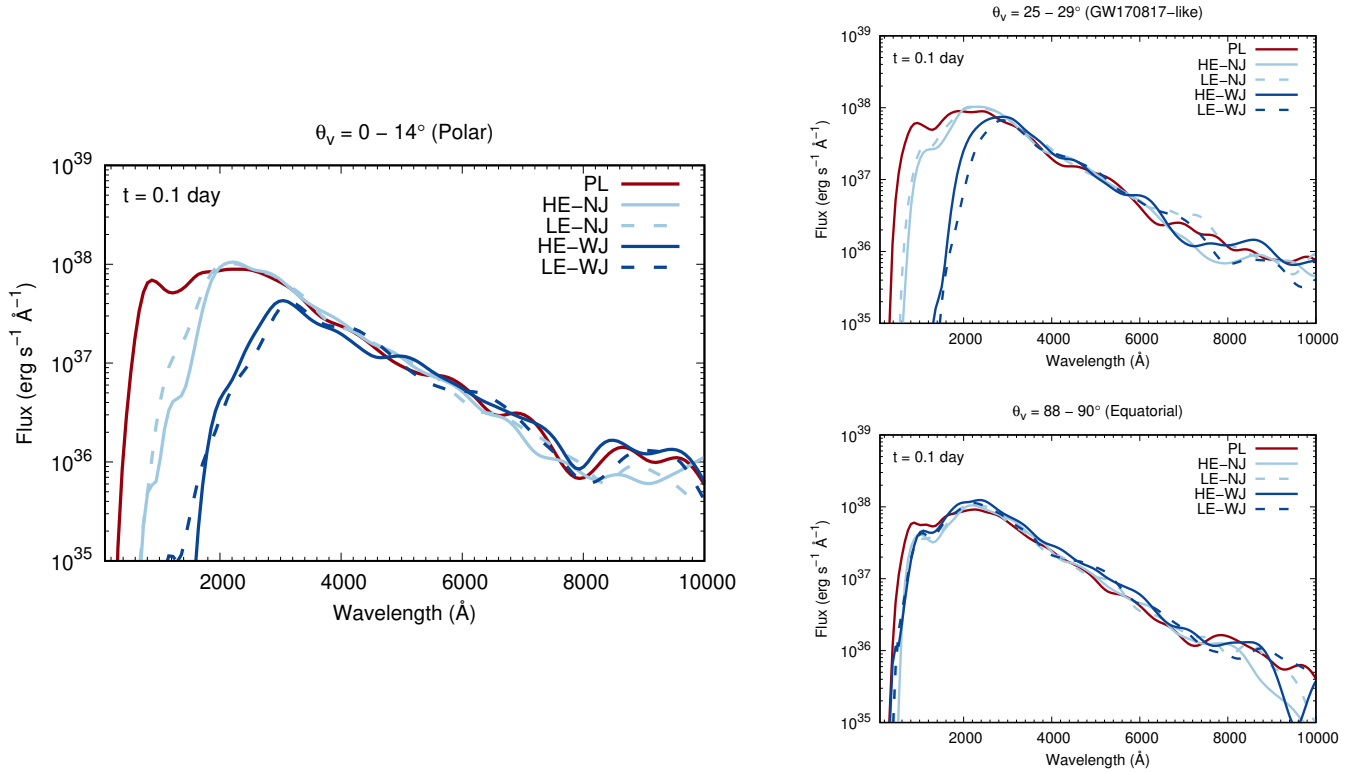


**Figure 4.** Kilonova spectra for different models at viewing angles: polar ( $\theta_v = 0-14^\circ$ , top left), GW170817-like ( $\theta_v = 25-29^\circ$ , top right), and equatorial ( $\theta_v = 88-90^\circ$ , bottom right). The spectral peak shifts towards longer wavelengths for the jet-interacted ejecta, especially for near-polar viewing angles. For the equatorial viewing angle, the differences almost vanish.

$\lambda = 100\text{--}35,000$ . These data are based on the opacity developed by Banerjee et al. (2020, 2024), which incorporate highly ionized (up to XI)  $r$ -process elements, enabling accurate treatment of early-time kilonova emission (starting  $t \sim 1$  hour) under high-temperature conditions.

The opacity increases as density decreases, as expected from Equation (3) and Equation (4). For example, at a fixed temperature of  $T = 40,000$  K, the maximum opacity varies from  $\kappa \sim 2\text{ cm}^2\text{ g}^{-1}$  to  $\kappa \sim 200\text{ cm}^2\text{ g}^{-1}$ , depending on the density (Figure 3). In the thin outer layer, where the density can be as low as  $\rho \lesssim 10^{-14}\text{ g cm}^{-3}$  (Figure 2), the opacity can therefore be substantially higher than the values typically assumed in previous studies (e.g.,  $\kappa \sim 1\text{ cm}^2\text{ g}^{-1}$ ; Klion et al. 2021).

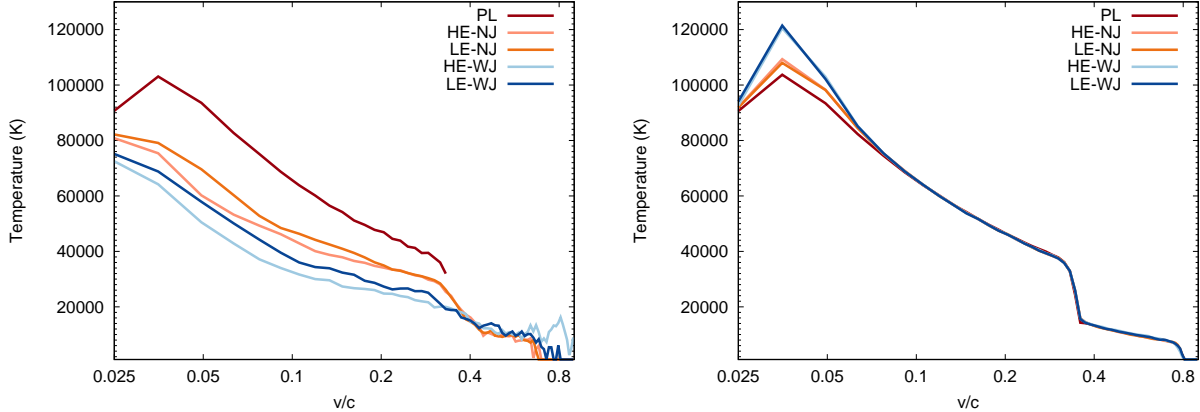
The variation of opacity with temperature is more complicated. With a change in temperature for a particular density, the ionization changes. For different ions, the energy level distribution is different. Depending on the energy level structure in the particular ions, the opacity values are varied (Banerjee et al. 2024). For more details on the temperature variation of opacity, see Tanaka et al. (2020); Banerjee et al. (2024).

## 4. RESULTS

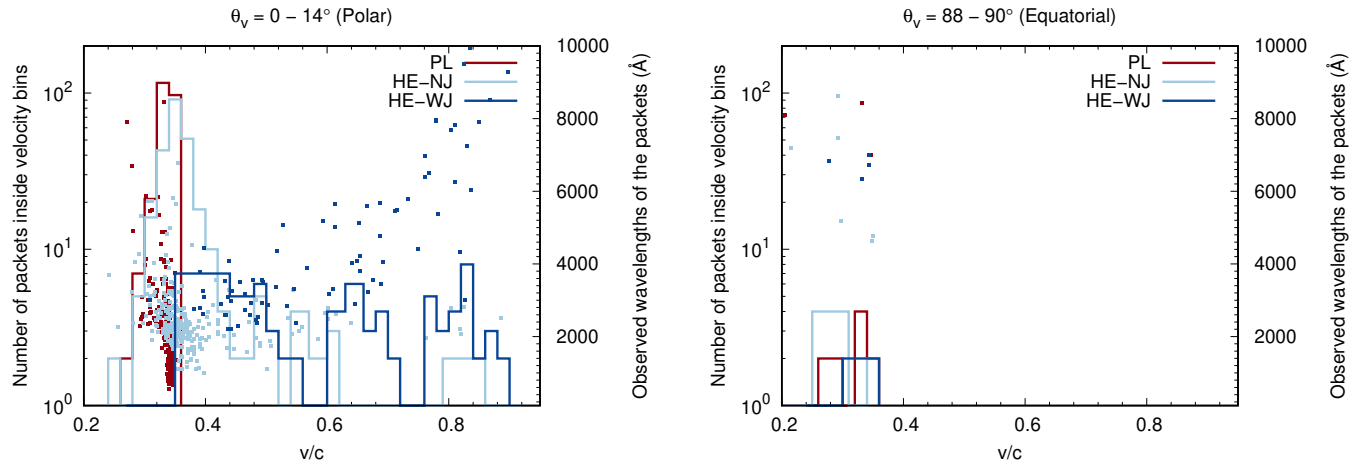
### 4.1. Spectra

Figure 4 shows the spectra at  $t = 0.1$  days for the different ejecta models, displayed for three representative viewing-angles measured from the pole:  $\theta_v = 0\text{--}14^\circ$  (polar),  $\theta_v = 25\text{--}29^\circ$  (GW170817-like; Finstad et al. 2018; Mooley et al. 2018), and  $\theta_v = 88\text{--}90^\circ$  (equatorial). At this early epoch, all models, independent of the viewing angle, exhibit spectral peaks in the short-wavelength ultraviolet regime ( $\lambda \approx 1,800\text{--}3,000\text{ \AA}$ ). However, both the detailed spectral shapes and the absolute flux levels vary significantly with viewing angle and ejecta model. Note that we focus on the global spectral shape rather than detailed features, as the current atomic data are not sufficiently accurate for the feature identification.

The origin of the spectral peaks at shorter wavelengths can be understood from the temperature structure at  $t = 0.1$  days (Figure 5). The temperature, shown for both the polar and equatorial directions, peaks near the center and decreases outward in all models, consistent with the higher densities in the inner ejecta. In the polar direction, the temperature at  $v = 0.3c$  ranges between  $T \approx 20,000\text{--}40,000$  K across the models, while the temperatures in the inner layers are higher. Even at higher



**Figure 5.** Temperature profiles for the different models at  $t = 0.1$  days are shown along the polar ( $\theta_v = 0\text{--}14^\circ$ , left) and equatorial ( $\theta_v = 88\text{--}90^\circ$ , right) directions. The jet-interacted ejecta exhibit modified temperature structures, reflecting the modified densities caused by the jet interaction, particularly along the polar direction. At high velocities in the polar region, these deviations are the strongest in the wide-jet models, consistent with their more significant modification of the thin outer layer. In contrast, along the equatorial direction, temperature differences are small, except in the innermost ejecta, where minor changes arise from weak density perturbations induced by the jet.



**Figure 6.** Distribution of the ejecta velocities at which photon packets undergo their final interaction before escaping. The points represent the corresponding wavelengths of escaping photon packets (right-hand axis). The particular colors represent individual models. When a jet interacts with the ejecta (models NJ and WJ), the ejecta produces a thin layer in front of the ejecta. Consequently, the last-scattering sites of the photons lie at relatively higher velocities than in the PL model with no jet-ejecta interaction. Also, the wavelengths of the emitted photons are on the longer wavelength side for the jet-interacted ejecta models.

velocities (e.g.,  $v \gtrsim 0.4c$ ), the ejecta cools but can still reach temperatures as high as  $T \sim 15,000$  K (Figure 5). These elevated ejecta temperatures naturally shift the spectral energy distribution toward the ultraviolet at early times, resulting in peaks at shorter wavelengths.

The effect of jet-ejecta interaction on the spectra is strongest for near-polar viewing angles, as shown in Figure 4. At a given observing angle, the location of the spectral peak depends primarily on the jet opening angle: models with wider jet produce progressive shifts towards longer wavelengths relative to the PL model. For a polar observer ( $\theta_v = 0\text{--}14^\circ$ ), the PL, NJ, and

WJ models peak at approximately  $\lambda \simeq 1800, 2200$ , and  $3000$ , respectively. By contrast, models with the same jet opening angle but different jet powers (e.g., HE-NJ versus LE-NJ) show only minor differences, and the peak wavelength remains largely unchanged.

The model-to-model differences diminish as the viewing angle increases. For polar viewing angles, the peak-wavelength separation between the PL and HE-WJ models is about  $\Delta\lambda \simeq 1200$ , while at a GW170817-like inclination ( $\theta_v \approx 25^\circ\text{--}29^\circ$ ), it decreases to  $\Delta\lambda \simeq 1000$  (top right panel of Figure 4). For equatorial viewing angles, the spectral differences between the PL and jet-

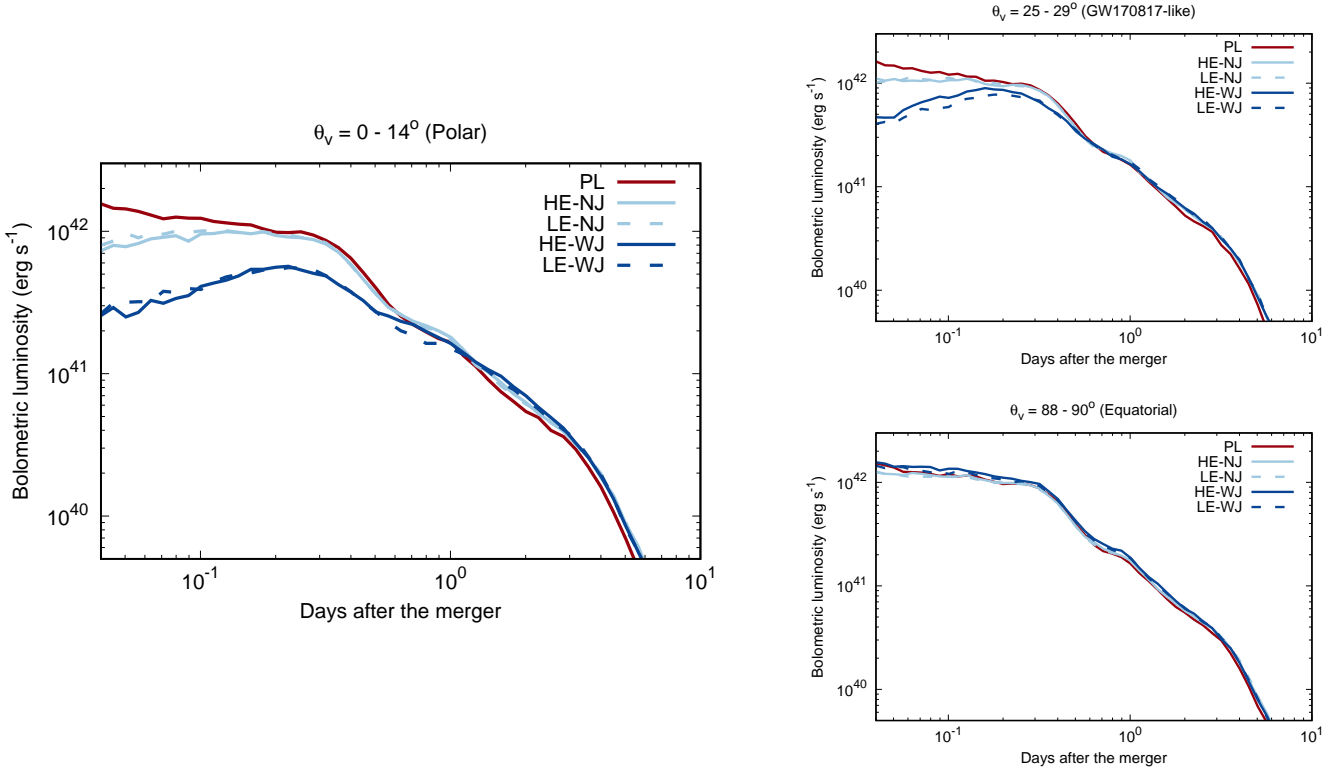


**Figure 7.** Bolometric light curves for different models shown in Table 1, with different panels representing different viewing angles. The presence of the jet makes the light curves dimmer, with the signature most pronounced in the polar direction ( $\theta_v = 0 - 14^\circ$ ). The wider jet (WJ) models show a stronger effect on light curves.

interacted models become negligible (bottom right panel of Figure 4).

To diagnose the origin of the differences in peak wavelength across models, we examine the physical conditions of the ejecta at the locations where photons undergo their final interaction (last scattering or absorption) before escaping. Figure 6 maps the velocity distribution (the histogram) and escape wavelengths (points) of the escaping photon packets. For simplicity, we consider only the high-energy jet models (HE), as the low-energy (LE) models exhibit similar behavior. Moreover, we show only photons escaping toward the polar and equatorial directions, displayed in the left and right panels of Figure 6, respectively.

When a jet interacts with the ejecta (models NJ and WJ), the ejecta produces a thin layer in front of the ejecta. Consequently, the last-scattering sites of the photons lie at relatively higher velocities than in the PL model with no jet-ejecta interaction. For instance, the photon escape in the polar direction happens at around  $v_{ej} \sim 0.35c$ , whereas the same for the models NJ and WJ are much higher ( $v_{ej} \sim 0.4 - 0.8c$ , Figure 6). Although the velocity from where the majority of the photons escape is not largely different for PL and NJ models ( $v_{ej} \sim 0.32c$  and  $v_{ej} \sim 0.36c$ , respectively), it can be as

high as  $v_{ej} \sim 0.8c$  for WJ model (Figure 6). This is due to higher opacity at thinner layers formed in the jet-interacted models (see Figure 3).

In the polar direction, the faster-moving ejecta, which are characterized by lower densities, have cooler temperatures than the dense inner regions because of the reduced total radioactive energy deposition (Figure 5). For example, in the wide-jet (WJ) models, the temperature in the thin outer layer at  $v_{ej} \sim 0.6c$  reaches only  $T \sim 15,000$  K at  $t \sim 0.1$  days. In contrast, for the PL model, the temperature at the outer edge of the ejecta from which photons escape (e.g., at  $v_{ej} \sim 0.32c$ ) reaches  $T \sim 40,000$  K at the same epoch (Figure 5). Consequently, in the jet-interacted models, especially in the wide-jet case, the ejecta layers from which photons escape are significantly cooler, shifting the spectral peak toward longer wavelengths. This effect is also reflected in Figure 6, where the escape wavelengths of individual photon packets (points) are more broadly distributed for the wide-jet model.

For the equatorial direction, the physical properties of the ejecta from where the photons are absorbed and re-emitted before finally escaping the ejecta are not significantly different among models (right panel, Figure 6). For instance, for the models, PL and HE-WJ,

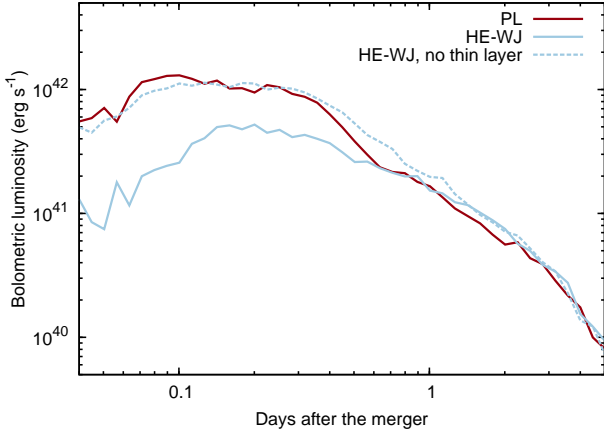


**Figure 8.** The bolometric luminosities at the polar viewing angle ( $\theta_v = 0 - 14$  degree) for the model HE-WJ with (solid blue) and without (dashed blue) the thin layer created at  $v_{ej} > 0.35c$  by the jet-ejecta interaction. By artificially removing the thin layer, the curves are almost identical to the light curves calculated using the ejecta with no jet interaction (PL, red curve).

the maximum velocity of the ejecta where the majority of the photons interacted before leaving the ejecta is  $v_{ej} \sim 0.35c$ . This is because the ejecta is not significantly affected around this region by the jet (Figure 1). The temperature around the equatorial region for all the different models is the same ( $T \sim 40,000$  K, Figure 5). This is also evident from the distribution of the wavelengths in the escaped photons. Hence, the differences among the spectra almost completely disappear in the equatorial direction.

#### 4.2. Light curves

To examine the temporal evolution of the kilonova emission, we present the bolometric light curves for all models in Figure 7, with different panels corresponding to different viewing angles. The presence of a jet suppresses the bolometric luminosity at early times ( $t \lesssim 1$  day), with the strongest effect occurring for polar viewing angles. For example, at  $t \sim 0.1$  days, the wide-jet model (HE-WJ) is fainter by a factor of  $\sim 2.5$  in bolometric luminosity compared to the no-jet (PL) model when viewed from the polar direction. This contrast decreases with increasing viewing angle: at a GW170817-like inclination, it is reduced to a factor of  $\sim 1.7$ , and it becomes negligible for equatorial observers (Figure 7), consistent with the spectra seen in Figure 4.

The fainter polar light curves can be attributed to the presence of a thin outer layer oriented toward the polar direction (Figure 2). A similar thin-layer effect has been reported for simpler ejecta configurations by Kasen et al.

(2017) and Banerjee et al. (2024). In our models, this thin layer is produced by the interaction between the jet and the ejecta and is characterized by low density and a lower temperature than the inner layers, leading to enhanced opacity (Figure 3). As a result, at early times most photons escape from this optically thick outer layer (Figure 6), yielding fainter emission in the polar direction. No comparable thin layer forms in the equatorial direction, which explains why the equatorial light curves remain largely similar across different models.

To further elaborate on this interpretation, we recompute the light curves for the wide jet-interacted ejecta model (HE-WJ) after artificially removing the thin outer layer beyond the velocity edge of the power-law ejecta ( $v_{ej} > 0.35c$ ). With this layer removed, the polar light curve (dashed blue curve in Figure 8) becomes nearly indistinguishable from that of the no-jet model (red curve in Figure 8), particularly at early times, demonstrating that the thin outer layer is responsible for the suppressed polar emission.

Note that we have assumed the homogeneous abundance distribution to calculate the light curves. But in reality, the equatorial ejecta will have lower  $Y_e$  than assumed. Hence, this assumption can affect values of the light curves and spectra in the equatorial direction, although it does not alter the relative behavior of models with and without a jet.

The early emission is more sensitive to the jet opening angle than to the jet power. The differences in the light curves between the wide and narrow jet (WJ and NJ) models are much more than the high-energy (HE) and low-energy (LE) jet models, as also seen in the spectra. This is because the differences in the light curves stem from the thin outer layer formed during jet propagation. The jet power itself has only a weak influence on the formation of this layer, because it enters the jet propagation equations linearly (as  $L_j$  or  $L_{iso}$ ), whereas the jet opening angle enters quadratically, scaling as  $\theta_j^2$ . As a result, wide jets (WJ) sweep up and thermalize a much larger fraction of the ejecta, producing a more massive thin layer in comparison to narrow jets (NJ). This explains why HE and LE models yield nearly identical light curves and spectra, whereas WJ and NJ models show pronounced differences.

As time progresses, the light curves of the jet-interacted models (NJ and WJ) converge toward those of the no-jet model (PL), even for polar viewing angles. This occurs because the photosphere recedes deeper into the ejecta, where differences in the density and temperature structures between models become smaller, causing the signatures in the light curves to disappear. We note that our models adopt a relatively low ejecta mass ap-

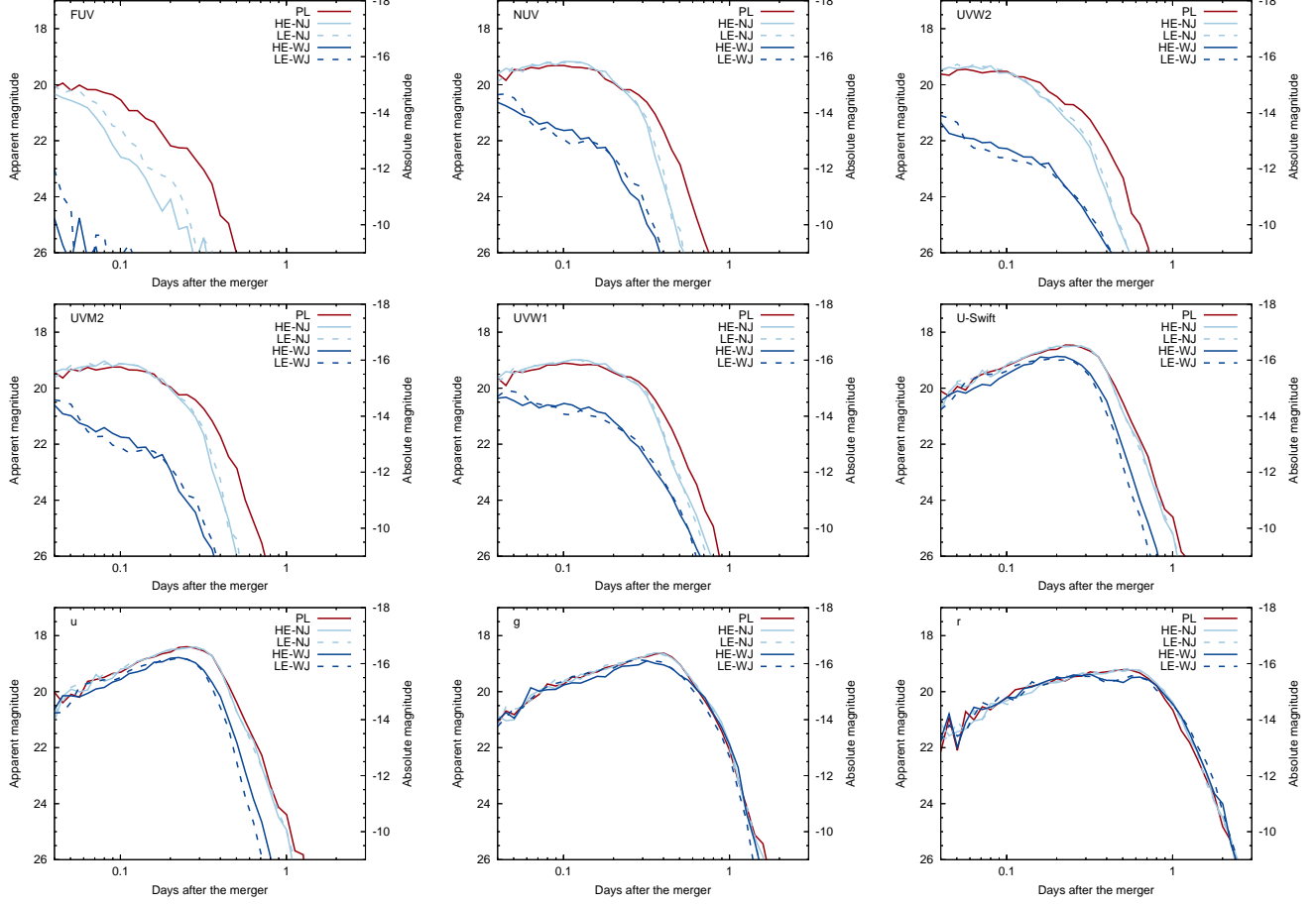


**Figure 9.** The multi-color light curves at polar viewing angles ( $\theta_v = 0-14^\circ$ ) for different models at 100 Mpc. Each panel shows distinct ultraviolet and optical filters, including *UVEX*: FUV ( $\lambda_{\text{Band}} = 1,3901,900$ ) and NUV ( $\lambda_{\text{Band}} = 2,0302,700$ ; calculated using v0.6.1 of the *UVEX* ETC); *Swift*: UVW2 ( $\lambda_{\text{Band}} = 1,597 - 3,480$ ), UVM2 ( $\lambda_{\text{Band}} = 1,699 - 2,964$ ), UVW1 ( $\lambda_{\text{Band}} = 1,614 - 4,730$ ), U ( $\lambda_{\text{Band}} = 3,018 - 4,781$ ), *u* ( $\lambda_{\text{Band}} = 3,206 - 4,081$ ), *g* ( $\lambda_{\text{Band}} = 3,876 - 5,665$ ), and *r* ( $\lambda_{\text{Band}} = 5,377 - 7,055$ ). The imprint of jet-ejecta interaction is most pronounced in the UV, U-*Swift*, and *u*-bands.

propiate for the disk-wind component of binary neutron star mergers through which the jet propagates (Hamidani & Ioka 2023a,b). For larger ejecta masses, this effect would persist to later times owing to the longer diffusion timescale.

We also compute multi-color light curves (Figure 9) to quantify the impact of jet-ejecta interaction on the broadband emission. We focus primarily on the polar viewing angle, where differences in both spectra and light curves are most pronounced. We present results in several representative ultraviolet and optical filters (*UVEX* NUV, FUV; *Swift* UVW2, UVW1, UVM2, U-*Swift*, *u*-, *g*-, and *r*-bands), as the early-time emission peaks at shorter wavelengths (Figure 4). Magnitudes are shown only for the polar orientation, where the observational signatures of the jet-ejecta interaction are maximally visible, consistent with the trends seen in the spectra and bolometric light curves.

We find that the impact of the jet-ejecta interaction is strongest in the ultraviolet and *u*-bands, while it becomes negligible in the *g*- and *r*-bands. For a given UV or *u*-band, the PL model is consistently the brightest, whereas the WJ models are the faintest. In the UVW2 band, for example, the UV luminosity for PL model reaches a peak of  $\simeq 19.5$  mag at  $t \simeq 0.15$  days for a source at 100 Mpc, while the WJ models produce fainter emission at the same epoch,  $\sim 22$  mag. Finally, we find that models with lower jet energies (LE) show only minor differences relative to their high-energy (HE) counterparts.

Among the ultraviolet bands, the jet-ejecta interaction produces the strongest signatures in the *UVEX* NUV, *Swift* UVW2, and UVM2 filters. We therefore recommend prioritizing follow-up observations in these bands to detect the imprint of the jet-ejecta interaction. The differences in the UV and *u*-band magnitudes persist only for a short period,  $t \lesssim 1$  day, implying that

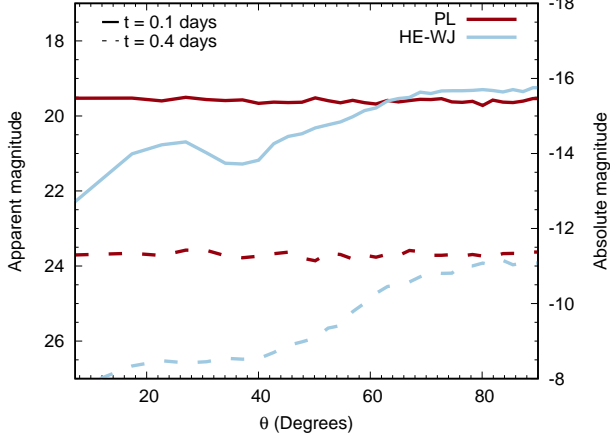


**Figure 10.** Variation of the UVW2-band apparent magnitude, shown for a source at a distance of 100 Mpc, with viewing angle at  $t = 0.1$  days (solid curves) and  $t = 0.4$  days (dashed curves). The signature of the jet–ejecta interaction remains clearly detectable out to viewing angles of  $\theta_v \simeq 60^\circ$ .

rapid follow-up after discovery is essential. Looking ahead, early-time ultraviolet observations with forthcoming facilities such as *ULTRASAT* (limiting magnitude  $\sim 22.4$  mag for 900 s exposure; Sagiv et al. 2014) and *UVEX* (limiting magnitude  $\sim 25$  mag for 900 s exposure; Kulkarni et al. 2021) will enable systematic measurements of early light curves, making it possible to robustly identify the observational signatures of jet–ejecta interaction.

Thus far, we have focused on the multi-color light curves viewed along the polar direction. To determine how far from the pole the signatures of jet–ejecta interaction remain observable, we examine the dependence of the *Swift* UVW2-band magnitude on viewing angle at  $t = 0.1$  days and  $t = 0.4$  days (solid and dashed curves in Figure 10) for the HE–WJ model. We find that the jet signature remains clearly detectable in the UVW2 band out to viewing angles of  $\theta_v \sim 60^\circ$ . This wide angular visibility allows the jet–ejecta interaction to be identified even when the afterglow, which is confined to narrower polar angles, is weak or undetectable. More on the observational implications of this result is discussed in the following section.

## 5. DISCUSSION

In this section, we compare our results with the other works (Section 5.1), and we discuss the conditions under which the jet signature in the earliest kilonova is visible beyond the afterglow resulting from the jet and the interstellar medium (ISM) interaction (Section 5.2).

### 5.1. Comparison with previous works

To place our results in the context of previous studies, we first consider the study by Klion et al. (2021), who have used the axisymmetric relativistic hydrodynamic models of Duffell et al. (2018) with the Monte Carlo radiative transfer code SEDONA (Kasen et al. 2006). Their work, similar to ours, examines how a relativistic jet affects kilonova ejecta and alters the emergent light curves. The principal difference between our works lies in the opacity treatment. While Klion et al. (2021) adopted a single, gray value of opacity ( $\kappa = 1 \text{ cm}^2 \text{ g}^{-1}$ ) to perform the radiative transfer simulations, we apply wavelength-, temperature-, and time-dependent opacities derived from detailed atomic data (Banerjee et al. 2020, 2022, 2024).

The effect of using constant gray opacities is clearly demonstrated by the different predictions obtained from the two works. For example, Klion et al. (2021) found that polar light curves are brighter than equatorial ones, attributing this to the fact that the ejecta, being modified by the jet, expose the hotter inner ejecta along polar viewing angles. This is contradictory to our results.

The discrepancy can be traced back to the treatment of the opacities in the two works. As Klion et al. (2021) have used a gray opacity with relatively lower constant value ( $\kappa = 1 \text{ cm}^2 \text{ g}^{-1}$ ), they find their photosphere residing near the hotter core in the polar direction. In contrast, in our models, the photosphere resides in a thin outer layer of the ejecta, as the opacity in this region is significantly enhanced by the low densities in the outermost layers (Figure 3). As a result, photons predominantly escape from this outer thin layer in jet-interacted ejecta (Figure 6), rather than from the hotter inner core along the polar direction at early times. As the thin layer has relatively low density, the overall energy deposition is lower than that of the highly dense bulk ejecta, causing the light curves in the polar direction to be fainter than those in the equatorial direction. The contrast underscores the sensitivity of kilonova observables to both the hydrodynamic structure and the detailed opacity.

To assess the impact of using wavelength-dependent opacities, we recalculated one of our models assuming a gray opacity of  $\kappa = 0.8 \text{ cm}^2 \text{ g}^{-1}$  (see Figure 11). This value was recommended by Banerjee et al. (2025) as providing the best match to the early-time bolometric light curves of light *r*-process kilonovae (Banerjee et al. 2024). However, as also emphasized by Banerjee et al. (2024), such a gray-opacity approximation fails to reproduce the multi-color light curves.

As shown in Figure 11, both the peak luminosity and the rise time of the polar (blue) and equatorial (red) light curves change substantially when switching

from wavelength-dependent opacities (solid lines) to a gray opacity (dashed lines). In the gray-opacity case, the magnitude difference between the polar and equatorial light curves is significantly reduced compared to the wavelength-dependent treatment. Moreover, the gray-opacity model produces a trend in which the polar light curve becomes brighter than the equatorial one at  $t \gtrsim 0.25$  days, consistent with the results of [Klion et al. \(2021\)](#). This behavior is not present when detailed opacities are used, demonstrating that reliance on gray opacities can be misleading when interpreting the signatures of jet–ejecta interaction.

Next, we compare our results with those of [Nativi et al. \(2021\)](#) and [Shrestha et al. \(2023\)](#). [Nativi et al. \(2021\)](#) model the hydrodynamic interaction between a narrow relativistic jet (opening angle  $\theta_j = 5^\circ$  and kinetic energies of  $E_k = 10^{49}$  erg and  $E_k = 10^{51}$  erg) and inject the jet in the neutrino-driven wind produced by a long-lived merger remnant; the wind profile is taken from [Perego et al. \(2014\)](#). They post-process the outflow with the Monte-Carlo radiative-transfer code **POSSIS** ([Bulla 2019](#)), adopting analytic opacity prescriptions developed based on [Tanaka et al. \(2018\)](#). Their synthetic light curves reproduce the trend reported by [Klion et al. \(2021\)](#), i.e., emission viewed along the polar axis is brighter than that seen from the equatorial plane, a consequence of the jet–ejecta interaction in the polar direction, altering the density structure in the polar direction, exposing the high-temperature inner ejecta.

[Shrestha et al. \(2023\)](#) refine the framework developed by [Nativi et al. \(2021\)](#) by recalculating the kilonova emission with the wavelength-dependent opacities of [Tanaka et al. \(2020\)](#). While this upgrade improves the results by showing the trend of equatorial light curves being brighter than the polar ones, the adopted opacity up to ion IV is not suitable to be used for the high-temperature ejecta at the early time ( $\lesssim 1$  day after merger). Hence, our calculations give a more accurate estimate for the earliest signal, especially in the ultraviolet wavelengths, relevant for the future satellites, such as *ULTRASAT* and *UVEX*.

## 5.2. Afterglow contamination

After the jet breaks out of the ejecta, it eventually propagates into the surrounding ISM. The interaction between the jet and the ISM produces an afterglow spanning a wide range of wavelengths. For an on-axis viewing angle, the afterglow peaks at early times, on a timescale comparable to that of the kilonova emission, and can outshine it. In such cases, the early kilonova emission with the imprint of the jet would not be observable. In contrast, for off-axis viewing angles, the afterglow emis-

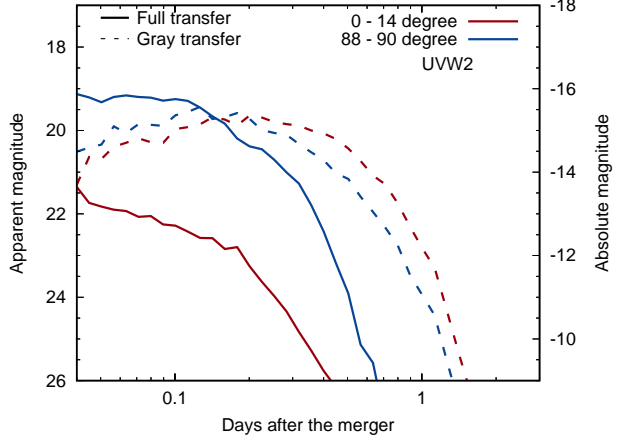


**Figure 11.** The UVW2 light curves for the HE–WJ model at polar ( $\theta_v = 0$ – $14^\circ$ ) and equatorial ( $\theta_v = 88$ – $90^\circ$ ) viewing angles for a source at 100 Mpc. We compare light curves calculated using wavelength-dependent opacities (solid curves) and gray opacity (dashed curves) with a value of  $\kappa = 0.8 \text{ cm}^2 \text{ g}^{-1}$ . In the gray-opacity case, the polar light curve becomes brighter than the equatorial one at  $t \gtrsim 0.2$  days. This is not physical, and is a consequence of using gray opacity, as can be understood from the results with detailed opacity.

sion is significantly dimmer, allowing the effects of the jet on the kilonova emission to be detected.

To evaluate the relative contributions of the afterglow and kilonova emission at off-axis viewing angles, we compute the afterglow signal using **afterglowpy** ([Ryan et al. 2020](#)). The code calculates afterglow light curves and spectra for different viewing angles based on a set of input parameters, including the jet energy and opening angle, the fractions of post-shock energy in accelerated electrons ( $\epsilon_e$ ) and magnetic fields ( $\epsilon_B$ ), and the interstellar medium (ISM) density ( $n$ ). The microphysical parameters (e.g.,  $\epsilon_e$ ) are chosen following the constraints derived from GRB170817A in [Troja et al. \(2018\)](#).

To compute the afterglow emission, we assume a Gaussian jet structure with a fixed opening angle of  $\theta_j = 18^\circ$ , chosen to match the wide-jet kilonova model (WJ), for which the jet signature is strongest. We consider both low- and high-energy jets (LE–WJ and HE–WJ models). This is because, although their kilonova emission is nearly identical, the afterglow contribution depends sensitively on the jet energy. We therefore adopt two jet luminosities,  $L_{\text{iso}} = 1 \times 10^{50} \text{ erg s}^{-1}$  for LE–WJ and  $L_{\text{iso}} = 5 \times 10^{50} \text{ erg s}^{-1}$  for HE–WJ.

In [Figure 12](#), we show the comparison between the afterglow at  $\theta_v = 14^\circ$  and the kilonova emission for the HE–WJ and LE–WJ models in the polar direction ( $\theta_v = 0$ – $14^\circ$ ) in the *Swift* UVW2 band. In both models,

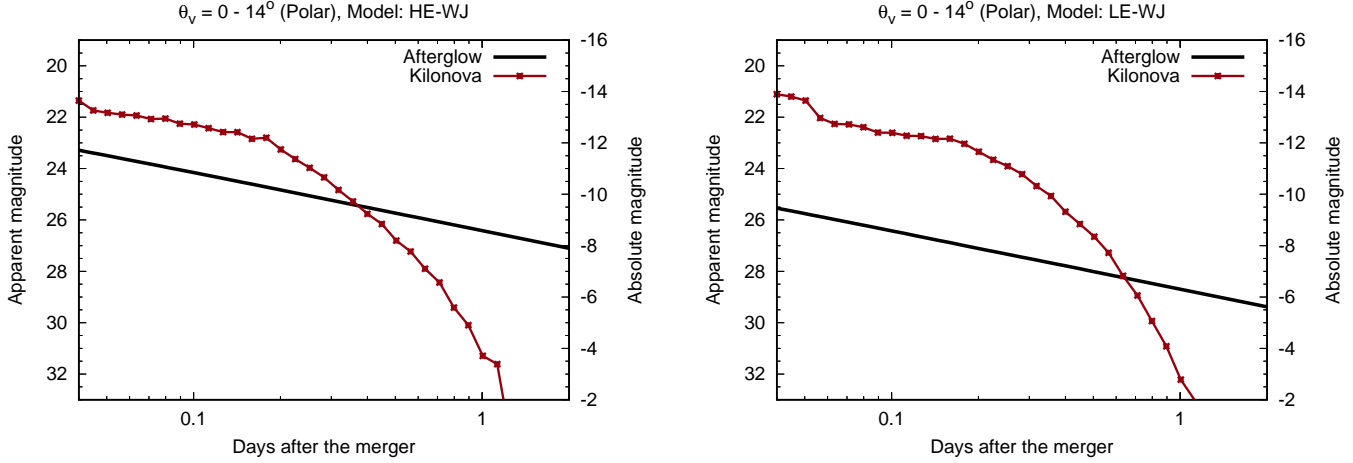


**Figure 12.** Afterglow emission in the UVW2 band for a structured Gaussian jet observed at a near-polar viewing angle ( $\theta_v = 14^\circ$ ). We adopt isotropic equivalent jet luminosities of  $L_{\text{iso}} = 10^{50} \text{ erg s}^{-1}$  (left) and  $5 \times 10^{50} \text{ erg s}^{-1}$  (right), with the jet opening angle fixed at  $\theta_j = 18^\circ$ , corresponding to the LE-WJ and HE-WJ jet models listed in Table 1. Other afterglow parameters are adopted from Troja et al. (2018):  $\theta_{\text{wing}} = 31.5^\circ$ ,  $p = 2.155$ ,  $\log_{10}(\epsilon_e) = -1.22$ ,  $\log_{10}(\epsilon_B) = -3.38$ ,  $\xi_N = 1.0$ , and  $d_L = 100 \text{ Mpc}$  and ISM densities of  $\log_{10}(n [\text{cm}^{-3}]) = -3.1$ . The corresponding kilonova light curves for HE-WJ (left) and LE-WJ (right) models are also shown for comparison in the same bands in the polar direction ( $\theta_v = 0 - 14^\circ$ ).

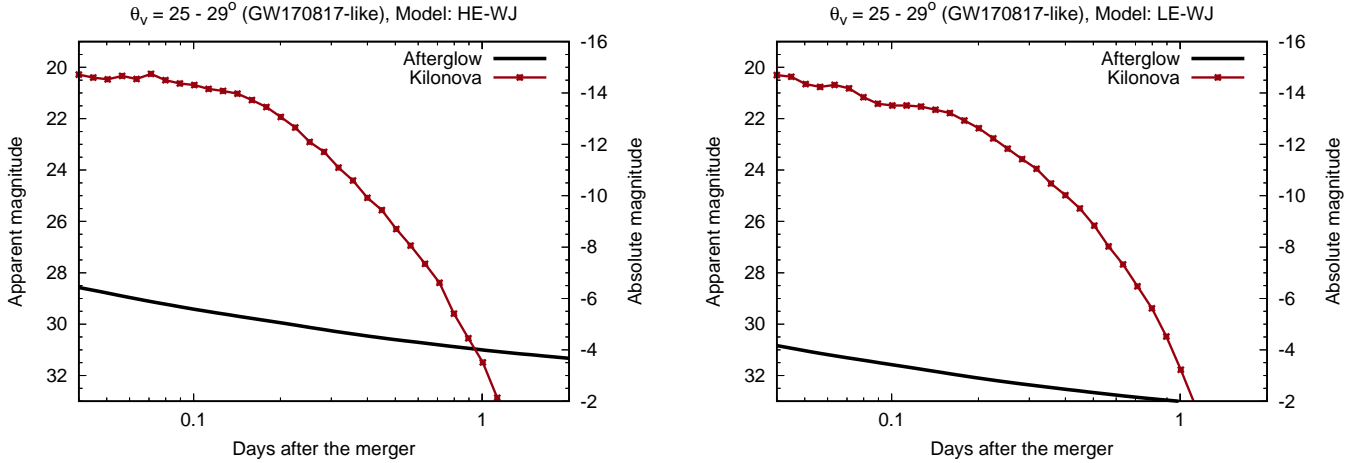


**Figure 13.** Same as Figure 12, but for an observer at a viewing angle of  $\theta_v = 29^\circ$ .

the kilonova is initially brighter than the afterglow during the first few hours. In the HE-WJ case, where the afterglow is stronger, the kilonova remains visible above the afterglow for approximately the first  $\sim 10$  hours, after which the afterglow dominates. In the LE-WJ model, the weaker afterglow allows the kilonova to remain visible for a longer period of about  $\sim 17$  hours. In the on-axis viewing angle, the afterglow will be brighter by  $\sim 2$  mag, as we found from a crude estimate by using *afterglowpy*. However, even in such a case, the early kilonova will be detectable in the earliest epochs ( $t \sim 7$  hours, Figure 12, Figure 13).

At larger viewing angles, the afterglow becomes much fainter because its emission declines more rapidly with

increasing angle than the kilonova emission. Consequently, for a GW170817-like viewing angle and the ISM density, the signature of the jet–ejecta interaction in kilonova is clearly detectable in the UV band during the first day, particularly for jets with wide opening angles (Figure 13).

## 6. CONCLUSION

We present the first radiative-transfer simulations of jet-interacted binary neutron star merger ejecta that incorporate detailed, wavelength-dependent opacities developed in Banerjee et al. (2020, 2024), which are suitable for early times ( $t \sim 1$  hour after merger). At a fixed temperature of  $T = 40,000 \text{ K}$ , representative of the outer edge of the bulk ejecta at  $t = 0.1$  days,

the maximum opacity for a lanthanide-free composition ( $Z = 20\text{--}56$ ) spans a wide range, from  $\kappa \sim 2 \text{ cm}^2 \text{ g}^{-1}$  to  $\kappa \sim 200 \text{ cm}^2 \text{ g}^{-1}$ , depending on the density (Figure 3). Using this detailed opacities, we investigate how jet–ejecta interaction affects kilonova light curves across a range of jet properties, varying the jet opening angle between  $\theta_j = 6.8^\circ$  and  $18^\circ$  (NJ and WJ models, Table 1) and the isotropic equivalent jet luminosity of  $L_{\text{iso}} = 10^{50}$  and  $5 \times 10^{50} \text{ erg s}^{-1}$  (LE and HE models, Table 1), using hydrodynamic simulations from Hamidani & Ioka (2023a,b).

Our study shows that the kilonova spectra at  $t = 0.1$  days (Figure 4) shift the spectral peak toward longer wavelengths in the jet-interacted models (NJ and WJ) compared to the model with no jet-interaction (PL). This effect is most prominent for polar viewing angles ( $\theta_v = 0\text{--}14^\circ$ ). This behavior arises because the jet–ejecta interaction forms a thin outer layer in front of the bulk ejecta (Figure 2), from which most photons escape at early times (Figure 6). This thin layer has a much lower density than the main ejecta, leading to reduced radioactive energy deposition and lower temperatures (Figure 5). As a result, the emission originates from cooler material, causing the spectral peak to shift to longer wavelengths. These differences largely disappear for equatorial viewing angles, where the jet has little impact on the ejecta structure.

Our bolometric light curves (Figure 7) show that jet–ejecta interaction suppresses the early-time ( $t \lesssim 1$  day) kilonova luminosity, with the strongest effect for polar viewing angles. At  $t \sim 0.1$  days, the wide-jet model (HE–WJ) is fainter by a factor of  $\sim 2.5$  than the no-jet (PL) model for polar observers, while this difference decreases to  $\sim 1.7$  at a GW170817-like inclination and becomes negligible for equatorial views, consistent with the spectra in Figure 4. This dimming is caused by the low-density, relatively cooler thin outer layer mainly in the polar direction (Figure 2). The physical conditions of this layer (density, temperature) make the opacity at this layer relatively high (Figure 3). This causes the photons at the early time to escape mainly from the thin outer layer. In contrast, the ejecta is only weakly affected by the jet in the equatorial direction, and no thin layer is created, leading to nearly indistinguishable light curves for the jet-interacted ejecta in that direction (Figure 7). At later times, all models converge as the photosphere recedes into deeper layers of the ejecta.

We compute multi-color light curves to quantify the impact of jet–ejecta interaction on the broadband emis-

sion, focusing on polar viewing angles where the signatures are strongest (Figure 9). The results are shown in representative ultraviolet and optical filters, reflecting the fact that the early-time emission peaks at short wavelengths (Figure 4). We show the multi-color light curves in the NUV and FUV bands of the upcoming satellite *UVEX*. In addition, we also show the results in *Swift* UVW2, UVW1, UVM2, and *U*; and the *u*-, *g*-, and *r*-bands. The jet–ejecta interaction produces its largest effects in the ultraviolet and *u*-bands, while differences become negligible in the *g*- and *r*-bands. In all UV and *u* filters, the PL model is consistently the brightest, and the WJ models are the faintest. For example, in the UVW2 band at 100 Mpc, the PL model reaches  $\simeq 19.5$  mag at  $t \simeq 0.15$  days, whereas the WJ models are fainter at the same epoch with  $\sim 22$  mag. The kilonova remains visible even beyond the afterglow at the earliest times for GW170817-like cases, particularly for lower-energy jets and for more off-axis viewing angles. Differences between high- and low-energy jet models (HE versus LE) are small, consistent with their nearly identical kilonova emission.

Among the ultraviolet bands, the strongest and most robust signatures of jet–ejecta interaction appear in the *UVEX* NUV and the *Swift* UVW2 and UVM2 filters, making these the highest-priority bands for follow-up. The differences in the UV and *u*-band light curves persist only for a short period ( $t \lesssim 1$  day), so rapid observations after discovery are essential. In the near future, forthcoming ultraviolet facilities such as *ULTRASAT* (limiting magnitude  $\sim 22.4$  mag in 900 s; Sagiv et al. 2014) and *UVEX* ( $\sim 25$  mag in 900 s; Kulkarni et al. 2021) will enable early-time UV monitoring for kilonovae, making it possible to robustly identify jet–ejecta interaction in future observations.

## ACKNOWLEDGMENTS

Numerical simulations presented in this paper were carried out with the computer facility in the Yukawa Institute for Theoretical Physics (YITP), Kyoto University, Japan. SB thanks Hannah Earnshaw and the *UVEX* team for providing the filters for the NUV and FUV bands. MT is supported by the Grant-in-Aid for Scientific research from JSPS (grant Nos. 23H00127, 23H04894, 23H04891, 21H04997, 23H05432) and the JST FOREST Program (grant No. JPMJFR212Y).

## REFERENCES

Abbott, B. P., Abbott, R., Abbott, T. D., et al. 2017, *PhRvL*, 119, 161101,  
doi: 10.1103/PhysRevLett.119.161101

Banerjee, S., Jerkstrand, A., Badnell, N., et al. 2025, arXiv e-prints, arXiv:2501.18345,  
doi: 10.48550/arXiv.2501.18345

Banerjee, S., Tanaka, M., Kato, D., & Gaigalas, G. 2024, *ApJ*, 968, 64, doi: [10.3847/1538-4357/ad4029](https://doi.org/10.3847/1538-4357/ad4029)

Banerjee, S., Tanaka, M., Kato, D., et al. 2022, *ApJ*, 934, 117, doi: [10.3847/1538-4357/ac7565](https://doi.org/10.3847/1538-4357/ac7565)

Banerjee, S., Tanaka, M., Kawaguchi, K., Kato, D., & Gaigalas, G. 2020, *ApJ*, 901, 29, doi: [10.3847/1538-4357/abae61](https://doi.org/10.3847/1538-4357/abae61)

Barnes, J., Kasen, D., Wu, M.-R., & Martínez-Pinedo, G. 2016, *ApJ*, 829, 110, doi: [10.3847/0004-637X/829/2/110](https://doi.org/10.3847/0004-637X/829/2/110)

Bauswein, A., Goriely, S., & Janka, H. T. 2013, *ApJ*, 773, 78, doi: [10.1088/0004-637X/773/1/78](https://doi.org/10.1088/0004-637X/773/1/78)

Bulla, M. 2019, *MNRAS*, 489, 5037, doi: [10.1093/mnras/stz2495](https://doi.org/10.1093/mnras/stz2495)

Connaughton, V., Goldstein, A., & Fermi GBM - LIGO Group. 2017, in American Astronomical Society Meeting Abstracts, Vol. 229, American Astronomical Society Meeting Abstracts #229, 406.08

Coulter, D. A., Foley, R. J., Kilpatrick, C. D., et al. 2017, *Science*, 358, 1556, doi: [10.1126/science.aap9811](https://doi.org/10.1126/science.aap9811)

Cowperthwaite, P. S., Berger, E., Villar, V. A., et al. 2017, *ApJL*, 848, L17, doi: [10.3847/2041-8213/aa8fc7](https://doi.org/10.3847/2041-8213/aa8fc7)

Drout, M. R., Piro, A. L., Shappee, B. J., et al. 2017, *Science*, 358, 1570, doi: [10.1126/science.aaq0049](https://doi.org/10.1126/science.aaq0049)

Duffell, P. C., Quataert, E., Kasen, D., & Klion, H. 2018, *ApJ*, 866, 3, doi: [10.3847/1538-4357/aae084](https://doi.org/10.3847/1538-4357/aae084)

Eichler, D., Livio, M., Piran, T., & Schramm, D. N. 1989, *Nature*, 340, 126, doi: [10.1038/340126a0](https://doi.org/10.1038/340126a0)

Fernandez, R., & Metzger, B. 2014, in AAS/High Energy Astrophysics Division #14, AAS/High Energy Astrophysics Division, 304.07

Fernández, R., & Metzger, B. D. 2013, *MNRAS*, 435, 502, doi: [10.1093/mnras/stt1312](https://doi.org/10.1093/mnras/stt1312)

Finstad, D., De, S., Brown, D. A., Berger, E., & Biwer, C. M. 2018, *ApJL*, 860, L2, doi: [10.3847/2041-8213/aac6c1](https://doi.org/10.3847/2041-8213/aac6c1)

Fong, W., Berger, E., Margutti, R., & Zauderer, B. A. 2015, *ApJ*, 815, 102, doi: [10.1088/0004-637X/815/2/102](https://doi.org/10.1088/0004-637X/815/2/102)

Freiburghaus, C., Rosswog, S., & Thielemann, F. K. 1999, *ApJL*, 525, L121, doi: [10.1086/312343](https://doi.org/10.1086/312343)

Fujibayashi, S., Kiuchi, K., Nishimura, N., Sekiguchi, Y., & Shibata, M. 2018, *ApJ*, 860, 64, doi: [10.3847/1538-4357/aabafd](https://doi.org/10.3847/1538-4357/aabafd)

Fujibayashi, S., Shibata, M., Wanajo, S., et al. 2020a, *PhRvD*, 101, 083029, doi: [10.1103/PhysRevD.101.083029](https://doi.org/10.1103/PhysRevD.101.083029)

—. 2020b, *PhRvD*, 102, 123014, doi: [10.1103/PhysRevD.102.123014](https://doi.org/10.1103/PhysRevD.102.123014)

Fujibayashi, S., Wanajo, S., Kiuchi, K., et al. 2020c, *ApJ*, 901, 122, doi: [10.3847/1538-4357/abafc2](https://doi.org/10.3847/1538-4357/abafc2)

Goldstein, A., Veres, P., Burns, E., et al. 2017, *ApJL*, 848, L14, doi: [10.3847/2041-8213/aa8f41](https://doi.org/10.3847/2041-8213/aa8f41)

Hamidani, H., & Ioka, K. 2023a, *MNRAS*, 520, 1111, doi: [10.1093/mnras/stad041](https://doi.org/10.1093/mnras/stad041)

—. 2023b, *MNRAS*, 524, 4841, doi: [10.1093/mnras/stad1933](https://doi.org/10.1093/mnras/stad1933)

Hamidani, H., Kiuchi, K., & Ioka, K. 2020, *MNRAS*, 491, 3192, doi: [10.1093/mnras/stz3231](https://doi.org/10.1093/mnras/stz3231)

Hotokezaka, K., Kiuchi, K., Kyutoku, K., & et al. 2013, *PhRvD*, 88, 044026, doi: [10.1103/PhysRevD.88.044026](https://doi.org/10.1103/PhysRevD.88.044026)

Just, O., Bauswein, A., Ardevol Pulpillo, R., Goriely, S., & Janka, H. T. 2015, *MNRAS*, 448, 541, doi: [10.1093/mnras/stv009](https://doi.org/10.1093/mnras/stv009)

Just, O., Kullmann, I., Goriely, S., et al. 2022, *MNRAS*, 510, 2820, doi: [10.1093/mnras/stab3327](https://doi.org/10.1093/mnras/stab3327)

Kasen, D., Badnell, N. R., & Barnes, J. 2013, *ApJ*, 774, 25, doi: [10.1088/0004-637X/774/1/25](https://doi.org/10.1088/0004-637X/774/1/25)

Kasen, D., Metzger, B., Barnes, J., Quataert, E., & Ramirez-Ruiz, E. 2017, *Nature*, 551, 80, doi: [10.1038/nature24453](https://doi.org/10.1038/nature24453)

Kasen, D., Thomas, R. C., & Nugent, P. 2006, *ApJ*, 651, 366, doi: [10.1086/506190](https://doi.org/10.1086/506190)

Kawaguchi, K., Fujibayashi, S., Shibata, M., Tanaka, M., & Wanajo, S. 2021, *ApJ*, 913, 100, doi: [10.3847/1538-4357/abf3bc](https://doi.org/10.3847/1538-4357/abf3bc)

Kawaguchi, K., Shibata, M., & Tanaka, M. 2018, *ApJL*, 865, L21, doi: [10.3847/2041-8213/aade02](https://doi.org/10.3847/2041-8213/aade02)

Kiuchi, K., Fujibayashi, S., Hayashi, K., et al. 2023, *PhRvL*, 131, 011401, doi: [10.1103/PhysRevLett.131.011401](https://doi.org/10.1103/PhysRevLett.131.011401)

Kiuchi, K., Kyutoku, K., Shibata, M., & Taniguchi, K. 2019, *ApJL*, 876, L31, doi: [10.3847/2041-8213/ab1e45](https://doi.org/10.3847/2041-8213/ab1e45)

Klion, H., Duffell, P. C., Kasen, D., & Quataert, E. 2021, *MNRAS*, 502, 865, doi: [10.1093/mnras/stab042](https://doi.org/10.1093/mnras/stab042)

Korobkin, O., Rosswog, S., Arcones, A., & Winteler, C. 2012, *MNRAS*, 426, 1940, doi: [10.1111/j.1365-2966.2012.21859.x](https://doi.org/10.1111/j.1365-2966.2012.21859.x)

Kouveliotou, C., Meegan, C. A., Fishman, G. J., et al. 1993, *ApJL*, 413, L101, doi: [10.1086/186969](https://doi.org/10.1086/186969)

Kromer, M., & Sim, S. A. 2009, *MNRAS*, 398, 1809, doi: [10.1111/j.1365-2966.2009.15256.x](https://doi.org/10.1111/j.1365-2966.2009.15256.x)

Kulkarni, S. R., Harrison, F. A., Grefenstette, B. W., et al. 2021, arXiv e-prints, arXiv:2111.15608, <https://arxiv.org/abs/2111.15608>

Lattimer, J. M., & Schramm, D. N. 1974, *ApJL*, 192, L145, doi: [10.1086/181612](https://doi.org/10.1086/181612)

Lazzati, D. 2020, *Frontiers in Astronomy and Space Sciences*, 7, 78, doi: [10.3389/fspas.2020.578849](https://doi.org/10.3389/fspas.2020.578849)

Levan, A. J., Gompertz, B. P., Salafia, O. S., et al. 2024, *Nature*, 626, 737, doi: [10.1038/s41586-023-06759-1](https://doi.org/10.1038/s41586-023-06759-1)

Li, L.-X., & Paczyński, B. 1998, *ApJL*, 507, L59, doi: [10.1086/311680](https://doi.org/10.1086/311680)

Lippuner, J., Fernández, R., Roberts, L. F., et al. 2017, MNRAS, 472, 904, doi: [10.1093/mnras/stx1987](https://doi.org/10.1093/mnras/stx1987)

Lucy, L. B. 2003, A&A, 403, 261, doi: [10.1051/0004-6361:20030357](https://doi.org/10.1051/0004-6361:20030357)

Metzger, B. D. 2020, Living Reviews in Relativity, 23, 1, doi: [10.1007/s41114-019-0024-0](https://doi.org/10.1007/s41114-019-0024-0)

Metzger, B. D., & Fernández, R. 2014, MNRAS, 441, 3444, doi: [10.1093/mnras/stu802](https://doi.org/10.1093/mnras/stu802)

Metzger, B. D., Martínez-Pinedo, G., Darbha, S., et al. 2010, MNRAS, 406, 2650, doi: [10.1111/j.1365-2966.2010.16864.x](https://doi.org/10.1111/j.1365-2966.2010.16864.x)

Miller, J. M., Ryan, B. R., Dolence, J. C., et al. 2019, PhRvD, 100, 023008, doi: [10.1103/PhysRevD.100.023008](https://doi.org/10.1103/PhysRevD.100.023008)

Mooley, K. P., Deller, A. T., Gottlieb, O., et al. 2018, Nature, 561, 355, doi: [10.1038/s41586-018-0486-3](https://doi.org/10.1038/s41586-018-0486-3)

Nativi, L., Bulla, M., Rosswog, S., et al. 2021, MNRAS, 500, 1772, doi: [10.1093/mnras/staa3337](https://doi.org/10.1093/mnras/staa3337)

Paczynski, B. 1991, AcA, 41, 257

Perego, A., Rosswog, S., Cabezón, R. M., et al. 2014, MNRAS, 443, 3134, doi: [10.1093/mnras/stu1352](https://doi.org/10.1093/mnras/stu1352)

Pinto, P. A., & Eastman, R. G. 2000, arXiv e-prints, astro. <https://arxiv.org/abs/astro-ph/0006171>

Rastinejad, J. C., Gompertz, B. P., Levan, A. J., et al. 2022, arXiv e-prints, arXiv:2204.10864. <https://arxiv.org/abs/2204.10864>

Rouco Escorial, A., Fong, W., Berger, E., et al. 2023, ApJ, 959, 13, doi: [10.3847/1538-4357/acf830](https://doi.org/10.3847/1538-4357/acf830)

Ryan, G., van Eerten, H., Piro, L., & Troja, E. 2020, ApJ, 896, 166, doi: [10.3847/1538-4357/ab93cf](https://doi.org/10.3847/1538-4357/ab93cf)

Sagiv, I., Gal-Yam, A., Ofek, E. O., et al. 2014, AJ, 147, 79, doi: [10.1088/0004-6256/147/4/79](https://doi.org/10.1088/0004-6256/147/4/79)

Savchenko, V., Ferrigno, C., Kuulkers, E., et al. 2017, ApJL, 848, L15, doi: [10.3847/2041-8213/aa8f94](https://doi.org/10.3847/2041-8213/aa8f94)

Sekiguchi, Y., Kiuchi, K., Kyutoku, K., & Shibata, M. 2015, PhRvD, 91, 064059, doi: [10.1103/PhysRevD.91.064059](https://doi.org/10.1103/PhysRevD.91.064059)

Shibata, M., & Hotokezaka, K. 2019, Annual Review of Nuclear and Particle Science, 69, 41, doi: [10.1146/annurev-nucl-101918-023625](https://doi.org/10.1146/annurev-nucl-101918-023625)

Shrestha, M., Bulla, M., Nativi, L., et al. 2023, MNRAS, 523, 2990, doi: [10.1093/mnras/stad1583](https://doi.org/10.1093/mnras/stad1583)

Smartt, S. J., Chen, T. W., Jerkstrand, A., et al. 2017, Nature, 551, 75, doi: [10.1038/nature24303](https://doi.org/10.1038/nature24303)

Sobolev, V. V. 1960, Soviet Ast., 4, 372

Tanaka, M., & Hotokezaka, K. 2013, ApJ, 775, 113, doi: [10.1088/0004-637X/775/2/113](https://doi.org/10.1088/0004-637X/775/2/113)

Tanaka, M., Kato, D., Gaigalas, G., & Kawaguchi, K. 2020, MNRAS, 496, 1369, doi: [10.1093/mnras/staa1576](https://doi.org/10.1093/mnras/staa1576)

Tanaka, M., Kato, D., Gaigalas, G., et al. 2018, ApJ, 852, 109, doi: [10.3847/1538-4357/aaa0cb](https://doi.org/10.3847/1538-4357/aaa0cb)

Tanvir, N. R., Levan, A. J., González-Fernández, C., et al. 2017, ApJL, 848, L27, doi: [10.3847/2041-8213/aa90b6](https://doi.org/10.3847/2041-8213/aa90b6)

Troja, E., Piro, L., Ryan, G., et al. 2018, MNRAS, 478, L18, doi: [10.1093/mnrasl/sly061](https://doi.org/10.1093/mnrasl/sly061)

Utsumi, Y., Tanaka, M., Tominaga, N., Yoshida, M., & et al. 2017, PASJ, 69, 101, doi: [10.1093/pasj/psx118](https://doi.org/10.1093/pasj/psx118)

Valenti, S., Sand, D. J., Yang, S., et al. 2017, ApJL, 848, L24, doi: [10.3847/2041-8213/aa8edf](https://doi.org/10.3847/2041-8213/aa8edf)

Wanajo, S., Müller, B., Janka, H.-T., & Heger, A. 2018, ApJ, 852, 40, doi: [10.3847/1538-4357/aa9d97](https://doi.org/10.3847/1538-4357/aa9d97)

Wanajo, S., Sekiguchi, Y., Nishimura, N., & et al. 2014, ApJL, 789, L39, doi: [10.1088/2041-8205/789/2/L39](https://doi.org/10.1088/2041-8205/789/2/L39)

Yang, S., Valenti, S., Cappellaro, E., et al. 2017, ApJL, 851, L48, doi: [10.3847/2041-8213/aaa07d](https://doi.org/10.3847/2041-8213/aaa07d)